

REPORT DOCUMENTATION PAGE				<i>Form Approved</i> OMB No. 0704-0188	
Public reporting burden for this collection of information is estimated to average 1 hour per response, including the time for reviewing instructions, searching existing data sources, gathering and maintaining the data needed, and completing and reviewing this collection of information. Send comments regarding this burden estimate or any other aspect of this collection of information, including suggestions for reducing this burden to Department of Defense, Washington Headquarters Services, Directorate for Information Operations and Reports (0704-0188), 1215 Jefferson Davis Highway, Suite 1204, Arlington, VA 22202-4302. Respondents should be aware that notwithstanding any other provision of law, no person shall be subject to any penalty for failing to comply with a collection of information if it does not display a currently valid OMB control number. PLEASE DO NOT RETURN YOUR FORM TO THE ABOVE ADDRESS.					
1. REPORT DATE (DD-MM-YYYY) 30/06/2008		2. REPORT TYPE FINAL		3. DATES COVERED (From - To) 4/2007 - 6/2008	
4. TITLE AND SUBTITLE High Performance Piezoelectric Airframes for Nano Air Vehicles				5a. CONTRACT NUMBER	
				5b. GRANT NUMBER FA9550-07-1-0367	
				5c. PROGRAM ELEMENT NUMBER	
6. AUTHOR(S) H. Kommepalli, H. Hirsh, C. Rahn, and S. Tadigadapa				5d. PROJECT NUMBER	
				5e. TASK NUMBER	
				5f. WORK UNIT NUMBER	
7. PERFORMING ORGANIZATION NAME(S) AND ADDRESS(ES) The Pennsylvania State University University Park, PA 16802				8. PERFORMING ORGANIZATION REPORT NUMBER	
9. SPONSORING / MONITORING AGENCY NAME(S) AND ADDRESS(ES) AFOSR, Arlington, VA				10. SPONSOR/MONITOR'S ACRONYM(S) AFOSR	
				11. SPONSOR/MONITOR'S REPORT NUMBER(S)	
12. DISTRIBUTION / AVAILABILITY STATEMENT Unlimited					
13. SUPPLEMENTARY NOTES					
14. ABSTRACT <p>Currently, Unmanned Air Vehicles (UAVs) are too large to penetrate buildings for situational awareness and reconnaissance, emplace important sensors, and sample and return material. While a variety of Micro Air Vehicles have been built and flown that use propellers and flapping wings for lift generation, Nano Air Vehicles (NAVs), defined as weighing less than 10 grams with wingspans less than 7.5 cm, have yet to be flown. NAV-scale actuators and wings with the requisite range of motion, power, and efficiency do not exist. In this project, we used a newly developed micromachining process based on Inductively Coupled Plasma Reactive Ion Etching (ICP-RIE), for PZT chips to fabricate novel, high performance actuators for NAVs. A novel T-beam actuator was fabricated using ICP-RIE etching from the front of a bulk PZT chip. Masked electrode deposition created active and passive regions in the PZT structure. With a T-shaped cross section, and bottom and top flange and web electrodes, a cantilevered beam can bend in-plane and out-of-plane with bimorph actuation in both directions. One of these T-beam actuators was fabricated and experimentally tested. An experimentally validated model predicted that the cross-section geometry can be optimized to produce higher displacement and blocking force.</p>					
15. SUBJECT TERMS Actuators, MEMS, PZT					
16. SECURITY CLASSIFICATION OF:			17. LIMITATION OF ABSTRACT Unlimited	18. NUMBER OF PAGES 16	19a. NAME OF RESPONSIBLE PERSON Christopher D. Rahn
a. REPORT Unclass.	b. ABSTRACT Unclass.	c. THIS PAGE Unclass.			19b. TELEPHONE NUMBER (include area code) 814-865-6237

High Performance Piezoelectric Airframes for Nano Air Vehicles

AFOSR Seed Grant No. FA9550-07-1-0367

Final Report

H. Kommepalli*, A. Hirsh[†], C. Rahn[‡], S. Tadigadapa[§]
The Pennsylvania State University

June 30, 2008

Abstract

Currently, Unmanned Air Vehicles (UAVs) are too large to penetrate buildings for situational awareness and reconnaissance, emplace important sensors, and sample and return material. While a variety of Micro Air Vehicles have been built and flown that use propellers and flapping wings for lift generation, Nano Air Vehicles (NAVs), defined as weighing less than 10 grams with wingspans less than 7.5 cm, have yet to be flown. NAV-scale actuators and wings with the requisite range of motion, power, and efficiency do not exist. In this project, we used a newly developed micromachining process based on Inductively Coupled Plasma Reactive Ion Etching (ICP-RIE), for PZT chips to fabricate novel, high performance actuators for NAVs. A novel T-beam actuator was fabricated using ICP-RIE etching from the front of a bulk PZT chip. Masked electrode deposition created active and passive regions in the PZT structure. With a T-shaped cross-section, and bottom and top flange and web electrodes, a cantilevered beam can bend in-plane and out-of-plane with bimorph actuation in both directions. One of these T-beam actuators was fabricated and experimentally tested. An experimentally validated model predicted that the cross-section geometry can be optimized to produce higher displacement and blocking force.

*Graduate Student

[†]Graduate Student

[‡]Professor of Mechanical Engineering

[§]Assoc. Professor of Electrical Engineering

1 INTRODUCTION

Piezoelectric actuators are used for many applications, including micropositioning systems, camera auto-focus lenses, structural vibration control, and control surfaces. Most piezoelectric actuators use Lead Zirconate Titanate (PZT) because it provides large piezoelectric and electromechanical coupling factors. To produce reasonable motion, however, the piezoelectric strain must be amplified. Stack actuators [1],[2],[3] produce larger motions by stacking electroded thin PZT disks and actuating through the thickness. In this case, the material poling, applied voltage and displacement are all in the same direction. This makes use of the d_{33} piezoelectric coefficient which is much larger than the d_{31} coefficient ($\sim 1/3$ of d_{33}) used in unimorph or bimorph actuators. In unimorph/bimorph actuators, two layers of material are separated by an electrode [3],[4],[5],[6]. The unimorph has one PZT layer poled through the thickness and a passive layer. The PZT layer expands through the thickness and contracts longitudinally when an electric field is applied. The longitudinal contraction causes the unimorph to bend due to the constraining passive layer. The bimorph substitutes a second active PZT layer for the passive layer. This produces maximum transverse displacement because each layer can be used with maximum applied field in the direction of poling. The maximum applied field in the direction opposite poling is limited to $\sim 1/3$ of the positive field to prevent depoling of the PZT. Tube actuators that produce bimorph actuation in two directions have been demonstrated at the macroscale [7].

At the microscale, stack and uni/bimorph actuators are difficult to fabricate. Although solder bonding techniques for PZT have been reported [8] stack actuators of more than a few layers have not been fabricated. Low performance AlN and ZnO [4],[9] and thin film PZT unimorph actuators have been made. The PZT films that have been demonstrated, however, do not have the quality of bulk PZT [10] and stress mismatch between the layers during the fabrication results in variably defected structures upon release. Thus, the performance of piezoelectric microactuators can be greatly improved.

Penn State University is well known for pioneering the development of piezoelectric ma-

terials, including high performance, PZT-based, single crystal PMN-PT and PZN-PT that are being produced by a spin-off company in State College. Since coming to PSU in 2000, Dr. Tadigadapa's research has combined this PZT materials expertise with his MEMS fabrication capabilities to produce innovative microactuators. Novel thin film unimorph [11], unimorph-flextensional [12], and bulk flextensional devices [13] have been fabricated in his laboratory. Dr. Rahn has collaborated with Dr. Tadigadapa to develop advanced, experimentally-validated models of the MEMS bulk flextensional devices [14][15] that enable model-based design and optimization.

Recently, Dr. Tadigadapa developed a new fabrication process that applies Inductively Coupled Reactive Ion Etching (ICP-RIE) directly to PZT to produce structures with vertical walls and flat faces [16]. Using multiple front and backside masks, ICP-RIE etches at various depths can produce a stair-stepped structure from the PZT or single crystal PMN/PZN-PT wafers (Minimum thickness = 100 μm). Masked metallization provides ground and power electrodes that activate specific areas in the structure to enable truly revolutionary MEMS devices. Dr. Tadigadapa has dedicated an RIE machine to this unique process – a process that is perfectly suited to the development of Nano Air Vehicle (NAV) airframes.

There is considerable interest in the development of NAVs for military operations. Current UAVs are too large to penetrate buildings for situational awareness and reconnaissance, emplacement of important sensors, and the sample/return of material. While a variety of Micro Air Vehicles have been built and flown that use propellers and flapping wings for lift generation, NAVs, defined as weighing less than 10 grams with wingspans less than 7.5 cm, have yet to be flown. Significant challenges remain in miniaturizing power, control, and communications, and, most importantly, NAV-scale actuators and wings with the requisite range of motion, power, and efficiency do not exist.

This final report for an AFOSR seed grant describes a new type of monolithic microactuator fabricated from bulk PZT by micro-machining using ICP- RIE process. Using this process we show that a two axis bimorph can be fabricated from a bulk PZT wafer. This

T-beam actuator is fabricated and experimentally shown to produce out-of-plane displacement. Model-based analysis shows that the T-beam actuator geometry can be optimized to produce large displacement and blocking force.

2 A NOVEL PZT FABRICATION PROCESS

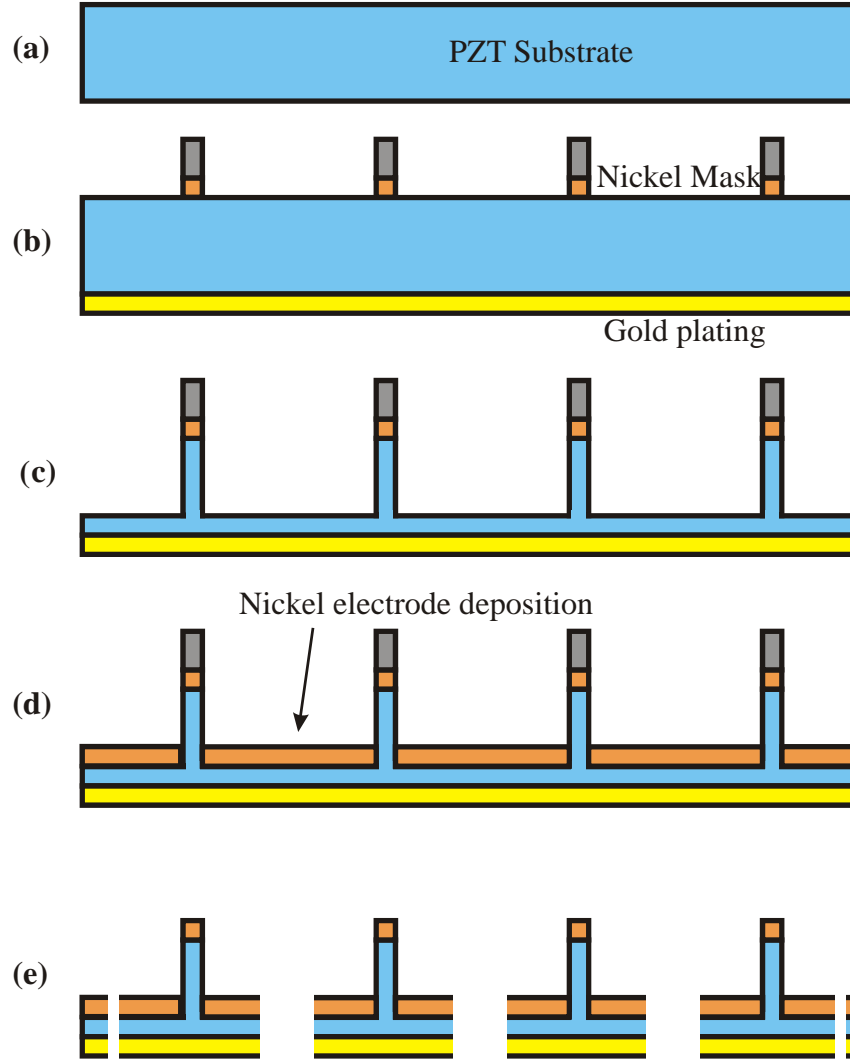


Figure 1: Schematic of the ICP-RIE fabrication process.

The first step in the ICP-RIE fabrication process involves lithographical patterning of a seed layer of Au/Cr onto fine lap finished PZT-4 substrates followed by electro-deposition of

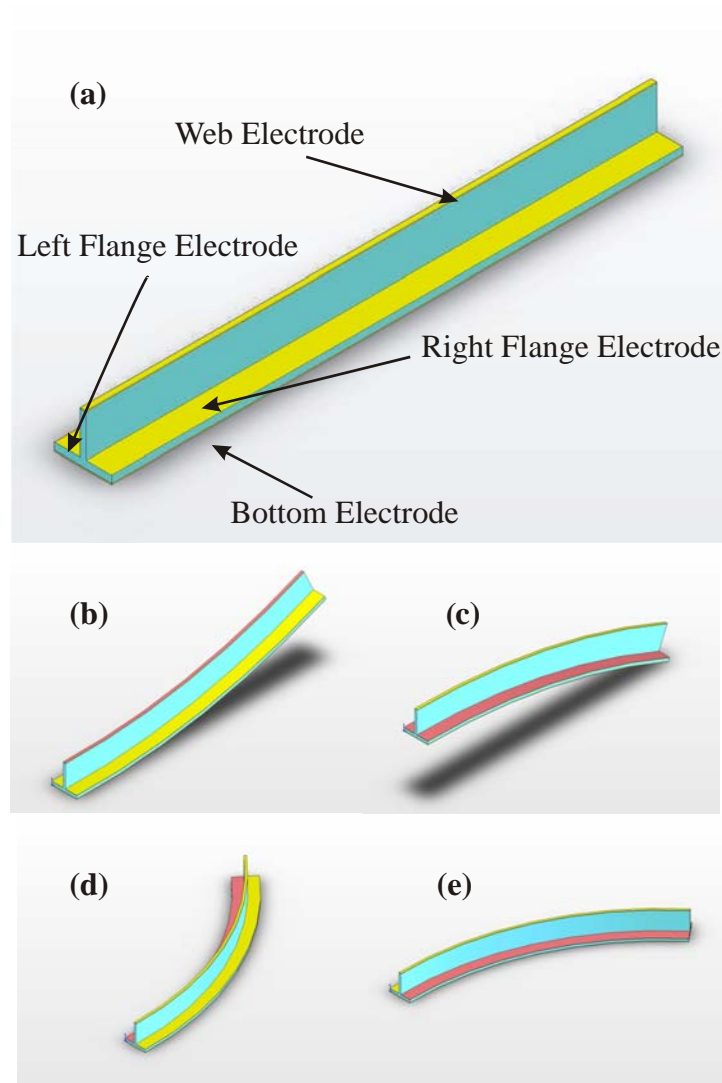


Figure 2: T-beam actuator concept: (a) As fabricated, and deflected shapes when voltage is applied between (b) flanges and bottom electrode, (c) web and bottom electrodes, (d) left flange and bottom electrodes, and (e) right flange and bottom electrodes.

18-22 μm thick nickel and chemical etching of the seed layer. The nickel acts as a hard mask during the etching process. A maximum etch rate of 19 to 25 $\mu\text{m/hr}$ on PZT is obtained using 2000 W of ICP power, 475 W of substrate power, 5 sccm of sulphur hexafluoride (SF_6), and 50 sccm of argon (Ar) on the PZT substrate. This high etch rate makes it possible to machine complex structures monolithically from PZT substrates. Multiple masks and etching from both top and bottom can produce stair stepped structures with arbitrary in-plane shapes.

Fig. 1 shows the fabrication process for an example structure with a T-shaped cross-section. The figure shows a cross-sectional view for the realization of the structure via the etching process. One inch square and 100 μm thick double side polished PZT substrate is the starting material for the T-beam actuators. The cleaned PZT substrate is coated with 500 \AA of chromium, followed by a 2000 \AA layer of gold as shown in Fig. 1(a). Using an aligner, the Cr/Au seed layer is patterned and electroplated with a thick 18-22 μm Ni hard mask layer (Fig. 1 (b)). This is followed by the deep etching of the piezoelectric material to realize the T-shaped structure (Fig. 1(c)). Then, Cr/Au electrodes are coated on the top of the web and flange (Fig. 1(d)). The structures can then be released from the substrate either by a second through etch or by using a dicing saw.

3 THE T-BEAM ACTUATOR CONCEPT

The previous section shows that a T-shaped structure can be fabricated and electroded using the ICP-RIE process. In this section we show that a T-beam actuator fabricated using this process, can provide bimorph actuation in two directions. The T-beam actuator is cantilevered and has a T-shaped cross-section as shown in Fig. 2. The entire T-beam is PZT with electrodes deposited on the top of the web, the top of each flange, and the bottom of the flange. The PZT is poled through-the-thickness from top to bottom.

Fig. 2 shows that the T-beam actuator can be bent both in-plane and out-of-plane by selectively activating the various electrodes. The bottom electrode acts as a ground. Out-

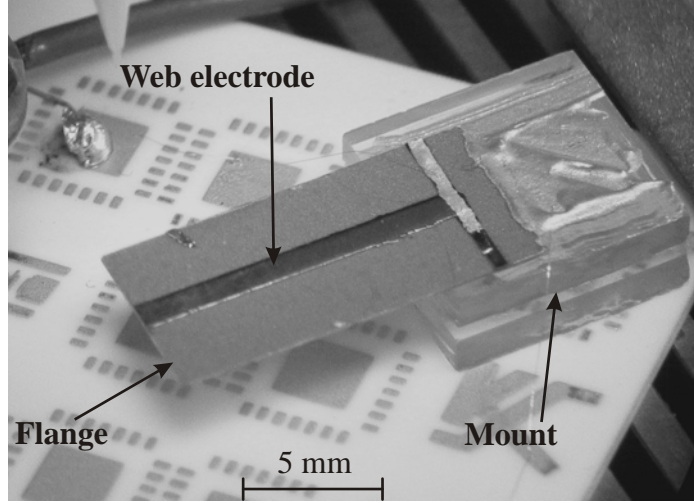


Figure 3: Photograph of the fabricated and mounted T-beam actuator with web top and flange bottom electroded.

of-plane motion can be achieved by applying voltage to the web electrode or to both flange electrodes. To maximize displacement we operate at maximum field in the direction of poling. Thus, for maximum deflection we actuate the web electrode at $V_w = h\phi_{\max}^+$ where h is the T-beam thickness and ϕ_{\max}^+ is the maximum field in the direction of poling. The web expands through the thickness and contracts longitudinally, through the d_{31} piezoelectric effect. The inactive flange constrains the lower part of the T-beam, acting as the passive layer in a bimorph design, and the beam bends upward (see Fig. 2(b)). Alternatively, if the two flanges contract due to actuation with $V = t\phi_{\max}^+$, then the web resists contraction and the T-beam bends downward (see Fig. 2(c)). The upward and downward displacement could be further increased by applying negative (rather than zero) voltage to the flanges ($V_G = -t\phi_{\max}^-$) and web ($V_W = -h\phi_{\max}^-$), respectively, effectively configuring it into a bimorph actuator. The maximum negative field (ϕ_{\max}^-), however, is typically limited to $\phi_{\max}^- \approx \phi_{\max}^+/3$. Hence, the bimorph T-beam design wherein maximum field can be applied for both upward and downward motion provides much larger displacement than with a single active layer.

The T-beam can also provide in-plane displacement by differential application of voltage to the two flanges. To bend left as shown in Fig. 2(d), the left flange electrode is actuated

at ($V_G = t\phi_{\max}^+$) and the right flange electrode has ($V_G = -t\phi_{\max}^-$). To bend right, the left and right flange electrode voltages are switched (see Fig. 2(e)).

4 EXPERIMENTAL RESULTS

To investigate the feasibility of the T-beam concept, we fabricate the T-beam shown in Fig. 3. The parameters of the fabricated T-beam are shown in Tab. 1. The T-beam is etched to a depth of $17\text{ }\mu\text{m}$ and released using a dicing saw. The T-beam is actuated by grounding the bottom electrode and applying voltage to the web electrode. The displacement of the T-beam actuator is measured using a laser vibrometer as a function of applied voltage. Fig. 5 shows the experimental displacement (Δ) versus applied voltage up to 270 V. The 8 mm long actuator produces a maximum displacement of $21.52\text{ }\mu\text{m}$.

5 MATHEMATICAL MODELING

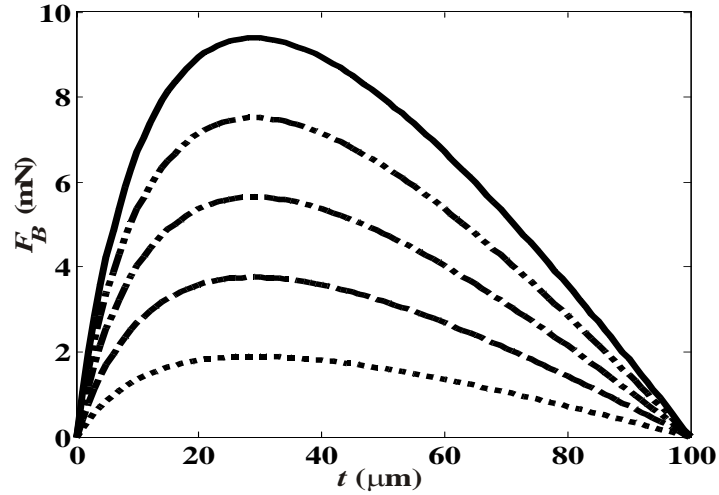


Figure 4: T-beam model: (a) the initial and deflected shape and (b) cross section

To optimize the performance of the T-beam actuator, we develop a model to predict out-of-plane displacement and blocking force. The T-beam actuator with the web and flange

electrodes shown in Fig. 4 is modeled as a cantilever beam using Euler-Bernoulli beam theory. Fig. 4(a) shows a schematic of the initial and deflected shapes of the T-beam actuator. The Cartesian coordinates x and z denote the horizontal and vertical position of the material particles, respectively. The variables u and w denote the displacements in the longitudinal and transverse directions, respectively. The cross-section of the T-beam shown in Fig. 4(b) has a flange width s , flange thickness t , web thickness b , and overall thickness h . The centroidal axis is at a distance

$$e = \frac{1}{2} \frac{t^2 s - t^2 b + 2tbh - bh^2}{ts - tb + bh}. \quad (1)$$

below the top of the flange. Voltage is applied between the web (V_W) or the two flange electrodes (V_G) and the bottom electrode. We assume a uni-axial electric field through the thickness of actuator as shown in Fig. 4(b). V_W and V_G are assumed to produce uniform fields only in the web and flanges, respectively. The potential energy is

$$\begin{aligned} U_b &= \int_{V_b} \frac{E}{2} \left(\frac{\partial u(x)}{\partial x} - z \left(\frac{\partial^2 w(x)}{\partial x^2} \right) \right)^2 dV, \\ U_p &= \int_{V_p} H dV, \\ U &= U_b + U_p, \end{aligned} \quad (2)$$

where E is the Young's modulus of PZT, U_b , U_p are the potential energy of the passive region and active region, respectively, and U is the total potential energy of the T-beam actuator.

The electric enthalpy H for the active piezoelectric material is given by

$$\begin{aligned} H &= \frac{E}{2} \left(\frac{\partial u(x)}{\partial x} \right)^2 + a_2 z^2 + a_{3M} \left(\frac{\partial^2 w(x)}{\partial x^2} \right)^2 + \\ &\quad a_{4M} \frac{\partial^2 w(x)}{\partial x^2} + a_{5M} - (a_{6W} - 2a_{2M}z) \frac{\partial^2 w(x)}{\partial x^2} \frac{\partial u(x)}{\partial x} \\ &\quad + a_{8M} \frac{\partial u(x)}{\partial x} \end{aligned} \quad (3)$$

Table 1: Parameters for T-beam actuator

Description	
Youngs modulus of PZT, E (GPa)	78
Flange thickness, t (μm)	83
Web width, b (mm)	1
Flange width, s (mm)	6
Actuator thickness, h (μm)	100
Actuator length, L (mm)	8
Piezoelectric strain coefficient, d_{31} (C/N)	-122e-12
Permittivity of PZT, ϵ_{33} ($C^2/(Nm^2)$)	1.15105e-08

Table 2: Area and moment of inertia for web actuation

Region	Area	Moment of inertia
Flange	$A_b = (s - b)t$	$I_{be} = \frac{1}{3} t (t^2 + 3e^2 - 3et)(s - b)$
Web	$A_p = bh$	$I_{pe} = \frac{bh^3}{12} + bh \left(\frac{h}{2} - t + e\right)^2$

where e_{31} is piezo-electric stress coefficient, ϵ_{33} is the permittivity of PZT, $M = W, G$ for web and flange actuation, respectively [5]. The coefficients in Eq. (3) are given by

$$\begin{aligned}
a_2 &= \frac{1}{2} \left(E + \frac{e_{31}^2}{\epsilon_{33}} \right), a_{3W} = -\frac{e_{31}^2 (2e + h - 2t)^2}{8\epsilon_{33}}, \\
a_{4W} &= -\frac{e_{31} V_W (2e + h - 2t)}{2h}, a_{5W} = \frac{-\epsilon_{33} V_W^2}{2h^2}, \\
a_{6W} &= \frac{e_{31}^2}{2\epsilon_{33}} (2e + h - 2t), a_{8W} = \frac{e_{31} V_W}{2h} \\
a_{3G} &= -\frac{e_{31}^2 (2e - t)^2}{8\epsilon_{33}}, a_{4G} = -\frac{e_{31} V_G (2e - t)}{2t}, \\
a_{5G} &= \frac{-\epsilon_{33} V_G^2}{2t^2}, a_{6G} = \frac{e_{31}^2}{2\epsilon_{33}} (2e - t), a_{8G} = \frac{e_{31} V_G}{2t}.
\end{aligned} \tag{4}$$

Substitution of Eqs. (2) into the principal of virtual work, $\int_0^t (\delta U + F \delta w(L)) dt = 0$, pro-

duces the field equations

$$\frac{d^4 w(x)}{dx^4} = 0, \frac{d^2 u(x)}{dx^2} = 0, \forall x \in (0, L), \quad (5)$$

geometric boundary conditions at the fixed end

$$w(0) = 0, \quad u(0) = 0, \quad \frac{dw(0)}{dx} = 0, \quad (6)$$

and the natural boundary conditions at the free end

$$\begin{aligned} (EI_{be} + 2a_2 I_{pe} + 2a_{3M} A_p) \frac{d^3 w(L)}{dx^3} - F &= 0, \\ (EI_{be} + 2a_2 I_{pe} + 2a_{3M} A_p) \frac{d^2 w(L)}{dx^2} + a_{4M} A_p &= 0, \\ E(A_b + A_p) \frac{du(L)}{dx} - a_{8M} A_p &= 0, \end{aligned} \quad (7)$$

where A_p , I_{pe} are the cross-sectional area and moment of inertia of the active region, and A_b , I_{be} are cross-sectional area and moment of inertia of the passive region, respectively, given in Tab. 2 (flip subscripts p to b and b to p for flange actuation). The solutions of Eqs. (5) are

$$\begin{aligned} w(x) &= c_3 x^3 + c_2 x^2 + c_1 x + c_0, \\ u(x) &= b_1 x + b_0. \end{aligned} \quad (8)$$

The 6 unknown coefficients c_i ($i = 0, 1, 2, 3$) and b_j ($j = 0, 1$) are solved analytically using the 6 boundary conditions to obtain

$$w(L) = -\frac{L^2(2FL + 3a_{4M} A_p)}{6(EI_{be} + 2a_2 I_{pe} + 2a_{3M} A_p)}. \quad (9)$$

The blocking force can be obtained by setting $w(L) = 0$ in Eq. (9) to produce

$$F_B = \frac{-3a_{4M} A_p}{2L} \quad (10)$$

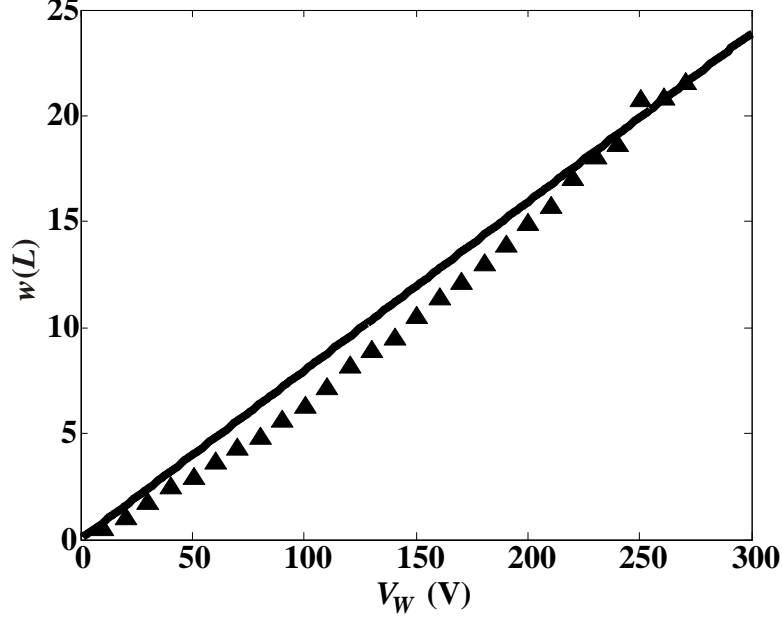


Figure 5: T-beam actuator experimental (\triangle) and theoretical (solid) displacement $w(L)$ versus applied voltage V_W for the actuator parameters shown in Tab. 1.

6 MODEL VALIDATION AND ACTUATOR DESIGN

Fig. 5 shows that the theoretically predicted T-beam displacement matches well with the experimentally measured displacement using the model parameters from Tab. 1 and $F = 0$. Thus, the model has been experimentally validated and it can be used to explore the design space for T-beam actuators. The design parameters include the geometric t , b , s , and h that define the cross section. Using the current fabrication process masks and wafer thickness, the web width, b , and actuator thickness, h , are constant. The flange thickness, t , and width, s , however can be reduced by using a longer etch time and dicing the actuator closer to the web, respectively. The displacement response can only be increased by $\sim 20\%$ with a narrower flange.

Fig. 6 plots the displacement at different applied voltages as a function of flange thickness t with the other parameters from Tab 1. The T-beam actuator has a maximum displacement of $w(L) \approx 120 \mu\text{m}$ for $t \approx 30 \mu\text{m}$ with $V_W = 250 \text{ V}$. The model predicts that the performance

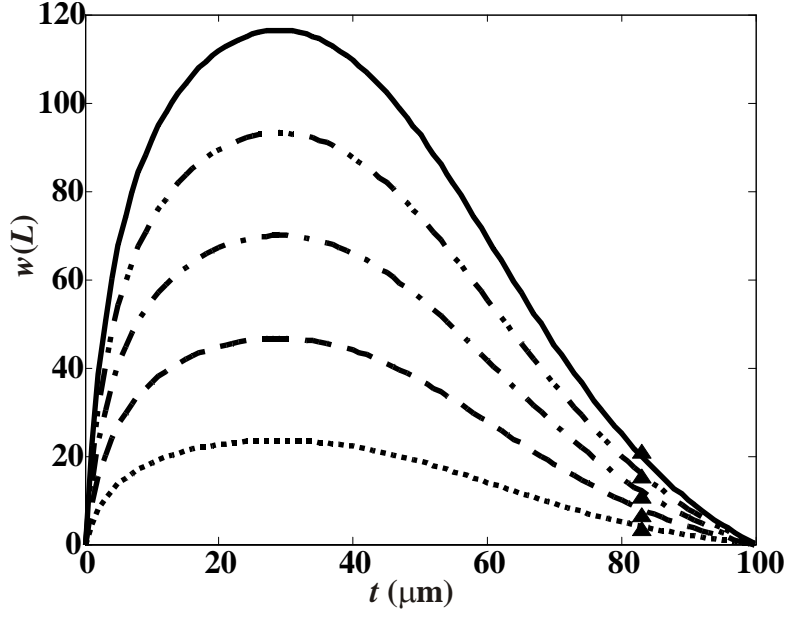


Figure 6: T-beam actuator displacement $w(L)$ versus flange thickness t for actuator parameters shown in Tab. 1 : Theoretical $w(L)$ for $V_W = 50$ V (dotted), 100 V (dashed), 150 V (dashed dotted), 200 V (dashed double dotted), 250 V (solid), and corresponding experimental $w(L)$ (\triangle).

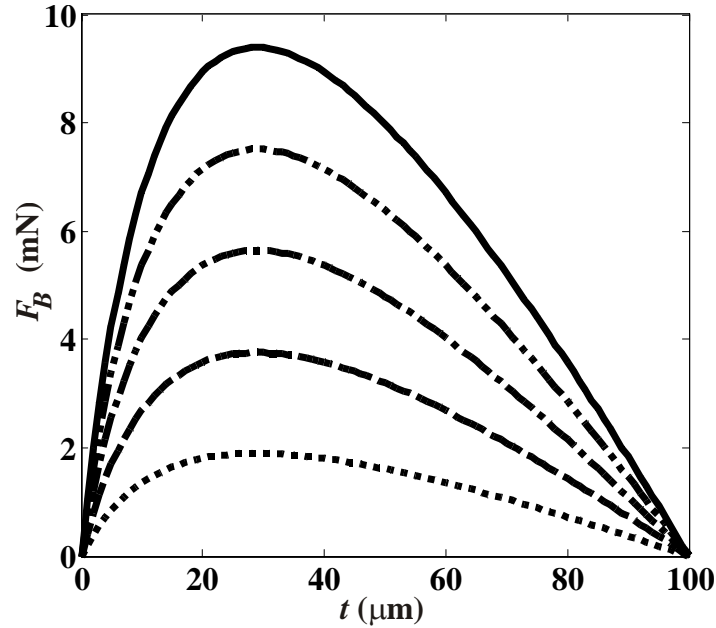


Figure 7: T-beam actuator blocking force (F_B) versus flange thickness t for actuator parameters shown in Tab. 1 : Theoretical F_B for $V_W = 50$ V (dotted), 100 V (dashed), 150 V (dashed dotted), 200 V (dashed double dotted), 250 V (solid).

can be improved by six times with a properly designed flange thickness.

Fig. 7 shows that the blocking force can also be optimized by reducing the flange thickness. The maximum blocking force $F_b \approx 9$ mN occurs at $t \approx 30$ μm , the same flange thickness that provides maximum displacement.

7 CONCLUSIONS

This seed grant project has shown that bulk PZT can be ICP-RIE etched to produce cantilevered structures with T-shaped cross sections. With voltage applied between electrodes on the top of the web and on the bottom of the flange, the T-beam actuation deflects out-of-plane. T-beam prototype produces 21.52 μm displacement at 270 V. The experimentally validated model shows that the displacement and blocking force can be maximized by decreasing the flange thickness. Work is currently underway to demonstrate bimorph actuation in-plane and out-of-plane using the flange electrodes. This work will be presented at IDETC 2008 and published in the conference proceedings. The results of this seed grant project indicate the potential of T-beam microactuators for NAV applications.

References

- [1] Giurgiutiu, V., and Rogers, C. A., 1996. “Energy based comparison of solid state induced strain actuators”. *Journal of Intelligent Material Systems and Structures*, **7**, January, pp. 4–14.
- [2] Giurgiutiu, V., Rogers, C. A., and Chaudhry, Z., 1997. “Design of displacement amplified induced-strain actuators for maximum energy output”. *Journal of Mechanical Design*, **119**, December, pp. 511–517.
- [3] Uchino, K., 2000. *Ferroelectric devices*. Marcel Dekker, New York.

- [4] Perçin, G., 2001. “Micromachined piezoelectrically actuated flextensional transducers for high resolution printing and imaging”. *IEEE Ultrasonics Symposium*, pp. 921–924.
- [5] Basak, S., Raman, A., and Garimella, S. V., 2005. “Dynamic response optimization of piezoelectrically excited thin resonant beams”. *Journal of Vibration and Acoustics*, **127**, pp. 18–27.
- [6] Wang, Q.-M., Du, X.-H., Xu, B., and Cross, L. E., 1999. “Electromechanical coupling and output efficiency of piezoelectric bending actuators”. *IEEE Transactions on Ultrasonics, Ferroelectrics, and Frequency control*, **46**(3), pp. 1947–1955.
- [7] Berg, M., Hagedorn, P., and Gutschmidt, S., 2004. “On the dynamics of piezoelectric cylindrical shells”. *Journal of Sound and Vibration*, **274**(1-2), July, pp. 91–109.
- [8] Goyal, A., Cheong, J., and Tadigadapa, S. A., 2004. “Tin-based solder bonding for mems fabrication and packaging applications”. *Journal of Micromechanics and Micro-engineering*, **14**(6), June, pp. 819–825.
- [9] Cheong, J., Goyal, A., Tadigadapa, S. A., and Rahn, C. D., 2005. “Fabrication and performance of a flextensional microactuator”. *Journal of Micromechanics and Micro-engineering*, **15**, pp. 1947–1955.
- [10] Gross, S. J., Tadigadapa, S. A., Jackson, T. N., Trolier-McKinstry, S., and Zhang, Q. Q., 2003. “Lead-zirconate-titanate based piezoelectric micromachined switch”. *Applied Physics Letters*, **83**(1), July, pp. 174–176.
- [11] Gross, S., and et al., 2003. “Lead-zirconate-titanate-based piezoelectric micromachined switch”. *Applied Physics Letters*, **83**(1), pp. 174–176.
- [12] Cheong, J., Tadigadapa, S., and Rahn, C., 2005. “Mems flextensional actuator using lead zirconate titanate thin film”. *Proc. IEEE MEMS Conference*, **Miami Beach, FL**.

- [13] Cheong, J., Tadigadapa, S., and Rahn, C., 2004. “Piezoelectric micro-flextensional actuator”. *SPIE MEMS/MOEM Components*, **5344**(1), pp. 106–114.
- [14] Cheong, J., Tadigadapa, S., and Rahn, C., 2005. “Fabrication and performance of a flex-tensional microactuator”. *J. Micromechanics and Microengineering*, **15**(10), pp. 1947–1955.
- [15] Cheong, J., Tadigadapa, S., and Rahn, C., 2005. “Dynamic response of a piezoelectric flextensional microactuator”. *ASME IDETC*, **Long Beach, CA**.
- [16] Subasinghe, S., Goyal, A., and Tadigadapa, S., 2006. “High aspect ratio plasma etching of buld lead zirconate titanate”. *SPIE Micromachining and Microfabrication*, **XI**.